



A three-plate kinematic model for Lau Basin opening

Kirsten E. Zellmer and Brian Taylor

Department of Geology and Geophysics, School of Ocean Earth Science and Technology, University of Hawaii, Honolulu, Hawaii 96822 (kezellmer@lbl.gov; taylor@soest.hawaii.edu)

[1] **Abstract:** We present revised compilations of bathymetry, magnetization, acoustic imagery, and seismicity data for the Lau Basin and surrounds. We interpret these data to more precisely locate the plate boundaries in the region and to derive a three-plate kinematic model for the opening of the Lau Basin during the Brunhes Chron. Our tectonic model includes the Niuafo'ou microplate, which is separated from the Australian Plate along the Peggy Ridge-Lau Extensional Transform Zone-Central Lau Spreading Center and from the Tongan Plate along the newly discovered Fonualei Rift and Spreading Center. Our model shows that Australia-Tonga plate motion between 15.5°S and 19°S is partitioned across the microplate, and it resolves the former apparent conflict between geodetic versus seafloor spreading velocities. Regionally, this implies that the angular rate of opening of the Lau Basin has been faster than that of the Havre Trough to the south and that the rapid current rates of Pacific subduction at the Tonga Trench (~240 mm/yr at 16°S) have been sustained for at least 0.78 m.y.

Keywords: Lau Basin; plate kinematics; microplate; seafloor spreading; geodetic vectors.

Index terms: Marine geology and geophysics; plate tectonics; plate motions—recent; Pacific Ocean.

Received September 1, 2000; **Revised** January 25, 2001; **Accepted** March 1, 2001; **Published** April XX, 2001.

Zellmer, K. E., and B. Taylor, 2001. A three-plate kinematic model for Lau Basin opening, *Geochem. Geophys. Geosyst.*, vol. 2, Paper number 2000GC000106 [8651 words, 13 figures, 7 tables]. Published April XX, 2001.

1. Introduction

[2] The Tonga-Fiji region has been key to the understanding of Earth dynamics since the formulation of the plate tectonics paradigm [e.g., *Isacks et al.*, 1968]. The 11-km-deep Tonga Trench is the locus of fastest subduction [*Bevis et al.*, 1995], and the subducted Pacific lithosphere generates a majority of all deep earthquakes [*Isacks et al.*, 1968]. The Lau Basin (Figure 1) was the first back arc basin

to be recognized as a young ocean basin formed by splitting a volcanic island arc [*Karig*, 1970]. Although subsequent models of back arc basin evolution were often two-dimensional and thus assumed only two plates above the subducting lithosphere (see review by *Taylor and Karner* [1983]; also see *Parson and Wright* [1996]), *Chase* [1971] recognized the existence of multiple plates and triple junctions in the opening of the North Fiji Basin. After two decades of controversy

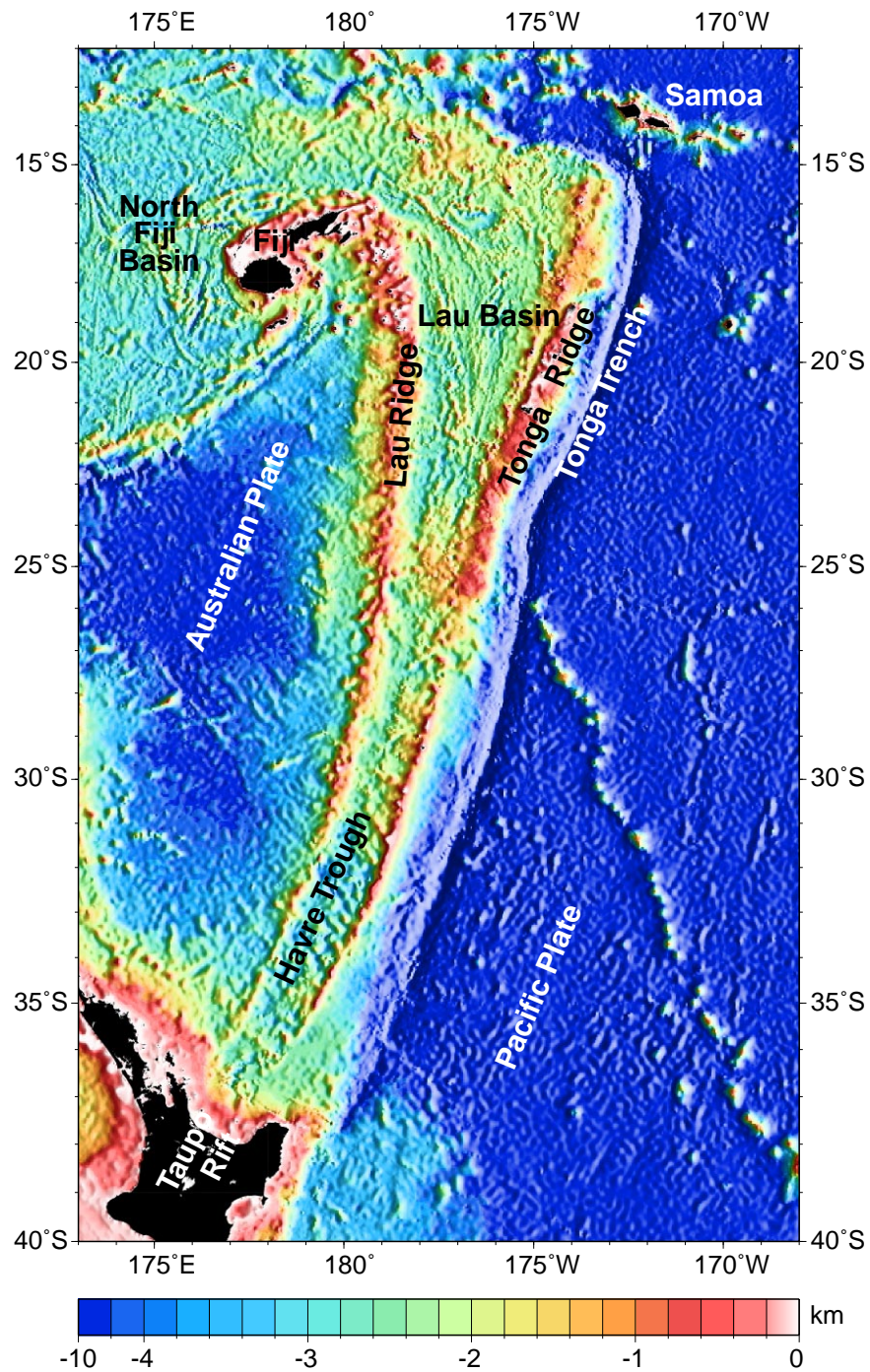
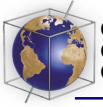


Figure 1. Regional bathymetric map showing the location of the Lau Basin and neighboring geologic features. The image is constructed from the predicted bathymetry of *Smith and Sandwell* [1997]; seafloor relief is shaded from the east, and islands are shown in black.

[Lawver *et al.*, 1976; Lawver and Hawkins, 1978; Weissel, 1977, 1981; Hamburger and Isacks, 1988; Parson and Hawkins, 1994], Taylor *et al.* [1996] used a magnetization inversion of bathymetry and magnetic data to definitively show that the opening of the Lau Basin was by seafloor spreading processes fundamentally similar to those occurring at mid-ocean ridges. Nevertheless, the tectonics of the Lau Basin region north of 18°S remained poorly understood, and Brunhes Chron spreading rates were reported to be only 75% of the opening rates measured geodetically [Bevis *et al.*, 1995]. Revised geodetic results [Bevis, 1997] partially closed the gap between the two data sets, but a quantitative kinematic model of Lau Basin opening has not been attempted previously.

[3] We use a set of recompiled bathymetry, magnetization, acoustic imagery, and seismicity data to define a multiple plate kinematic model that (1) explains a majority of the tectonic features throughout the Lau Basin, (2) is consistent with both spreading rates determined from the marine magnetic data and the revised geodetic velocities, and (3) satisfies rigid plate criteria. We address the recent tectonics (0.78 Ma to present) and implications of a three-plate system for Lau Basin opening.

2. Data Compilation

[4] We include new results from three systematic surveys to update the Lau Basin data compilation and magnetization inversion of Taylor *et al.* [1996]. R/V *Moana Wave* cruise MW9603 surveyed the basin from edge to edge between 17°S and 18°35'S. A R/V *Hakerei Maru 2* cruise (hereafter referred to as MMAJ9507) surveyed the spreading axis and nearby ridge flanks between 19°25'S and 22°S. R/V *Melville* cruise BMRG08MV principally surveyed the forearc region [Wright *et al.*, 2000]. Swath bathymetry and acoustic imagery

were collected using a Hydrosweep system on MMAJ9507, the HAWAII MR1 (HMR1) side scan system on MW9603, and a SeaBeam 2000 system on BMRG08MV. Surveys were navigated using the Global Positioning System (GPS). Detailed descriptions of these three surveys and their results will be published elsewhere (for BMRG08MV, see Wright *et al.* [2000]).

2.1. Bathymetry

[5] Using GMT [Wessel and Smith, 1991] and MB-system software [Caress and Chayes, 1995], we created a 0.002° (~200 m) grid of bathymetry (Figure 2). The compilation incorporates the MMAJ9507, MW9603, and BMRG08MV swath bathymetry with (1) the predicted bathymetry of Smith and Sandwell [1997], (2) data obtained from the U. S. National Geophysical Data Center (NGDC), (3) data obtained from the South Pacific Applied Geoscience Commission (SOPAC), (4) digitized contours of published bathymetry maps [Wiedicke and Collier, 1993; Wiedicke and Habler, 1993; Defense Mapping Agency, 1990a, 1990b], and (5) additional unpublished swath bathymetry data (R/V *Ewing* 9512 and 9914; R/V *Yokosuka* 9614, refer to Fujiwara *et al.* [2001]). The bathymetry compilation process was completed in stages similar to those described by Martinez *et al.* [1995] in order to obtain a grid that best merges all the data of varying quality and resolution. To achieve this end, all bathymetric data sets were first combined and median filtered in 1 arc min (~1.85 km) blocks to generate a regional base data set that smoothly merges with the more detailed data. This regional data set was then combined with the original data, median filtered in 0.002° blocks, and gridded at 0.002° node spacing. High-resolution swath data that were considered to be the most reliable and best navigated were given greatest priority within the grid.

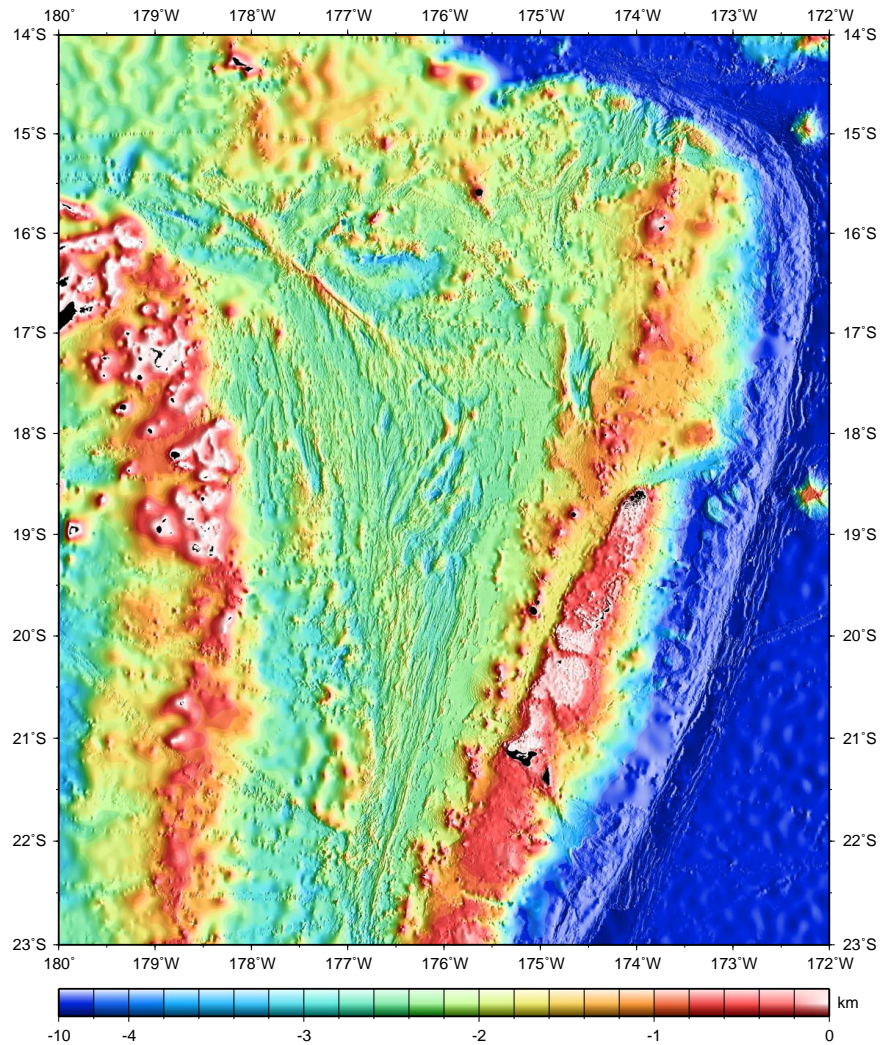


Figure 2. Bathymetry of the Lau Basin region, with seafloor fabric shaded from the east and islands filled in black. Systematic survey data from the MMAJ9507 and MW9603 cruises define the central part of the basin from 17°S to 22°S.

2.2. Magnetic Data and Magnetization Pattern

[6] Magnetic data from the MMAJ9507, MW9603, and BMRG08MV cruises were incorporated with other data available from the NGDC (Figure 3). Using compilation processes described by *Martinez et al.* [1995], we created a new 0.5 arc min (~900 m) grid of

magnetic anomaly data. A corresponding 0.5 arc min grid of sampled bathymetry was used in conjunction with the magnetic anomaly grid to produce an updated grid of the magnetization distribution (Figure 4) using the inversion method of *Parker and Heustis* [1974] as modified by *Macdonald et al.* [1980]. Despite applying average crossover corrections to the magnetics data, some track artifacts remain

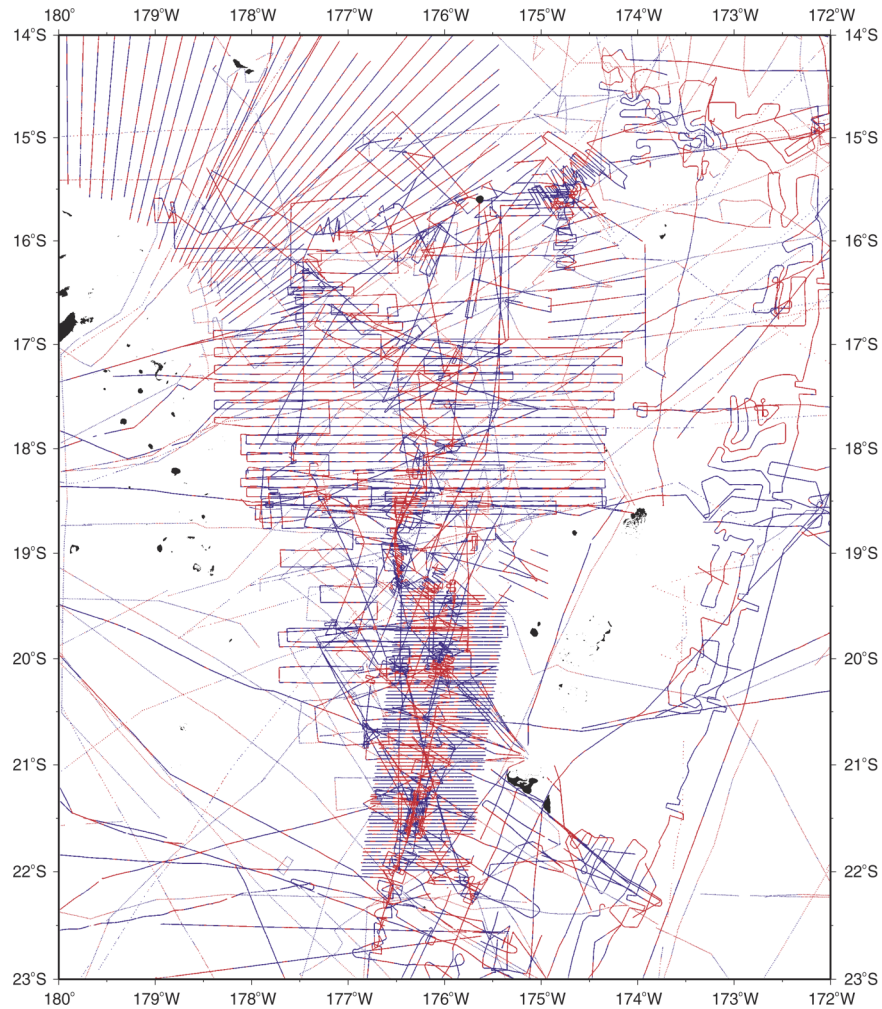
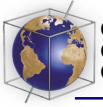


Figure 3. Track chart showing the location of magnetic anomaly data (red, positive; blue, negative) used in the magnetization inversion (Figure 4). Magnetic data from the MMAJ9507, MW9603, and BMRG08MV cruises were incorporated with other data available from the NGDC.

apparent in this higher-resolution grid. Parameters pertinent to the magnetization inversion were similar to those used by *Taylor et al.* [1996]: a 1-km-thick source layer was assumed, and wavelengths >325 km and <1 km were filtered out of the data. Areas shallower than 1 km were masked so as to satisfy the requirement that the magnetic source does not come within one grid cell of the observation surface [Parker, 1972].

2.3. Acoustic Imagery

[7] We compiled HMR1 side scan sonar imagery from MW9603 with MMAJ9507 Hydrosweep amplitude data and published GLORIA imagery from two cruises (HMAS *Cook* cruise CK8915 [Hughes Clarke *et al.*, 1993; Parson and Tiffin, 1993; Hill and Tiffin, 1993] and RRS *Charles Darwin* cruise CD3388 [Parson *et al.*, 1990, 1992]). The digital acous-

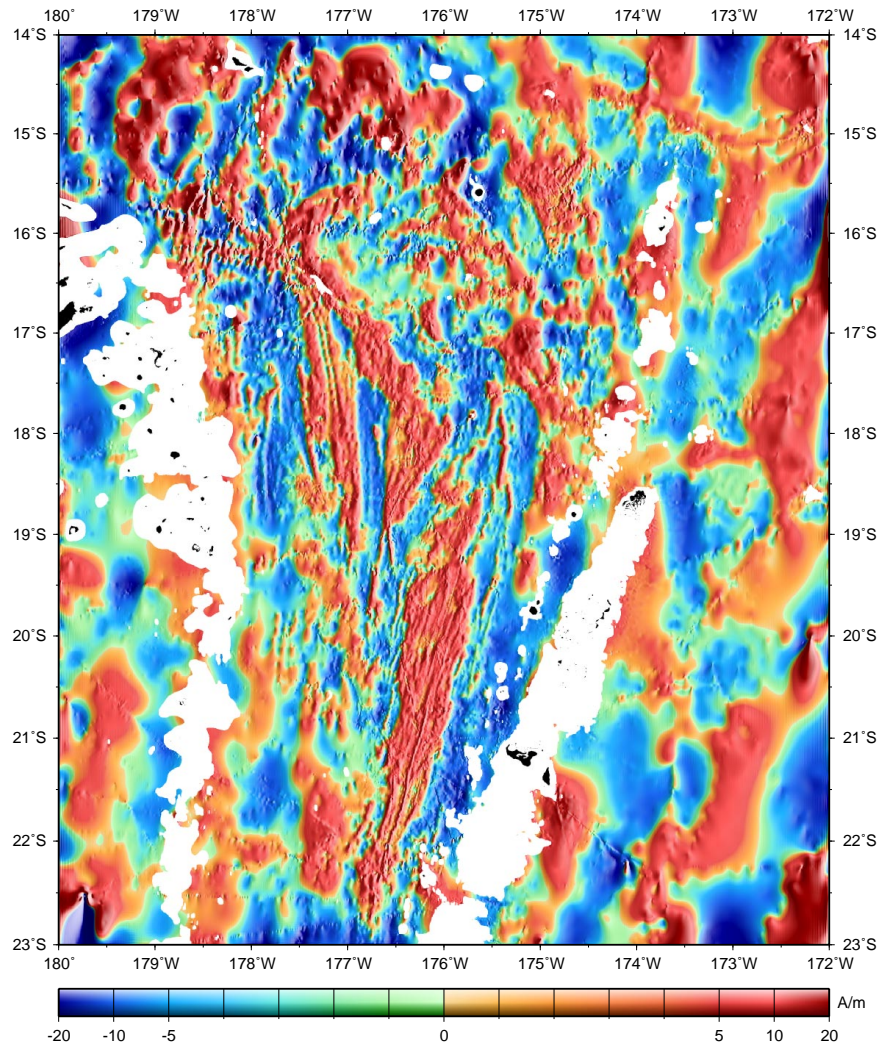


Figure 4. Seafloor magnetization of the Lau Basin region. The magnetization inversion assumes a 1-km-thick source layer underlying and conformable with the seafloor and is an updated version of that discussed by Taylor *et al.* [1996]. Areas where the seafloor is shallower than 1 km are masked.

tic imagery varies in quality as a function of the sonar frequency, resolution, and dynamic range of the three systems. In Figure 5 we used non-linear histogram normalization to make their acoustic reflectivity ranges appear similar.

2.4. Seismicity

[8] Three main earthquake seismicity data sets are plotted in Figure 5: (1) centroid moment

tensor (CMT) focal mechanisms [Pelletier *et al.*, 1998], (2) a set of shallow earthquakes (<50 km) from the International Seismological Center (ISC), and (3) microearthquake locations ascertained from an Ocean Bottom Seismometer (OBS) array deployed for 3 weeks in 1984 [Eguchi, 1987]. The microearthquake locations are limited to the vicinity of the OBS array, which was deployed between 17°S, 177°W and 18.5°S, 176°W.

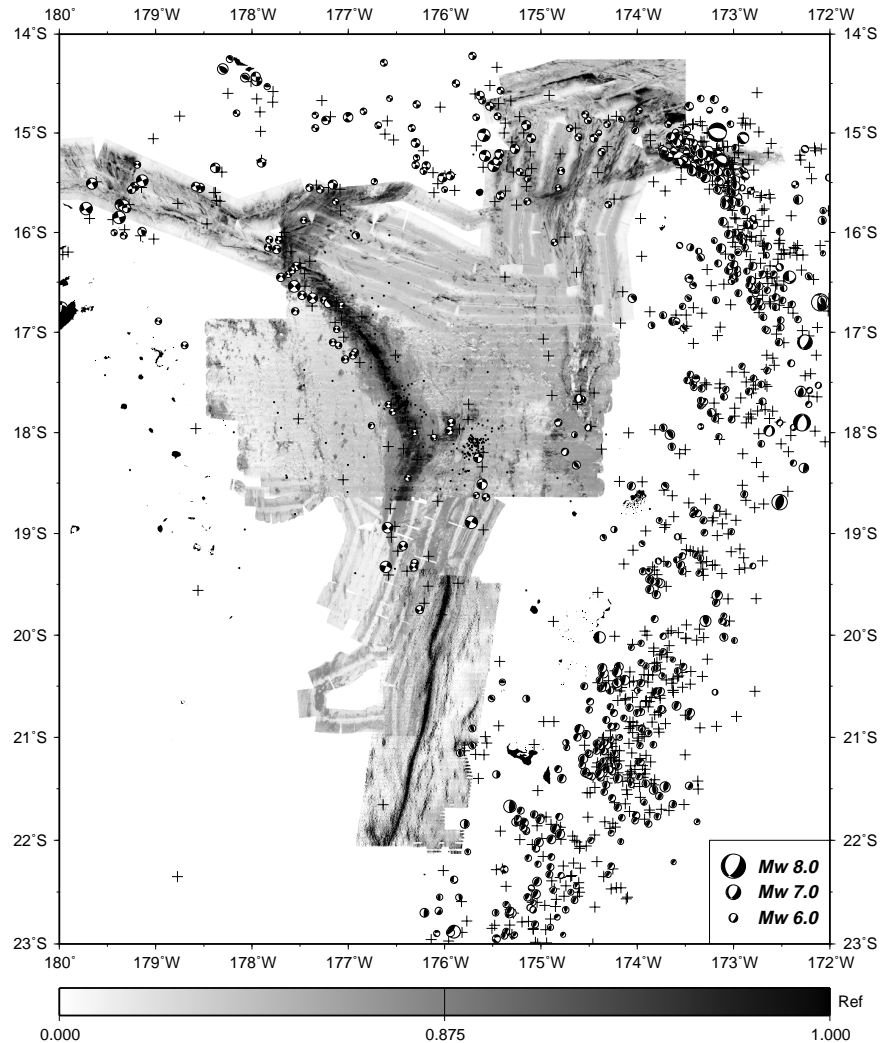
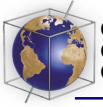


Figure 5. Acoustic reflectivity and seismicity of the Lau Basin region. The reflectivity scale (Ref) has been nonlinearly normalized between 0 (white, low reflectivity) and 1 (black, high reflectivity). CMT focal mechanisms [Pelletier *et al.*, 1998], ISC earthquakes of <50 km depth (crosses), and microearthquakes (small dots) located by an OBS array in the region between 17°S, 177°W and 18.5°S, 176°W [Eguchi, 1987] are included.

3. Observations at Proposed Plate Boundaries

[9] On the basis of the location of the strong acoustic reflectivity of the neovolcanic zones (Figure 5) and the detailed morphology now discernible in the bathymetry (Figure 2), we revise spreading center, transform fault, and

subduction zone locations throughout the region (Figure 6). We used contrast stretched versions of the acoustic imagery and enlarged versions of the bathymetry to precisely locate these boundaries. Here we briefly describe key observations along the main plate boundaries pertinent to this paper. More detailed descriptions of individual boundaries are in preparation for presentation elsewhere.

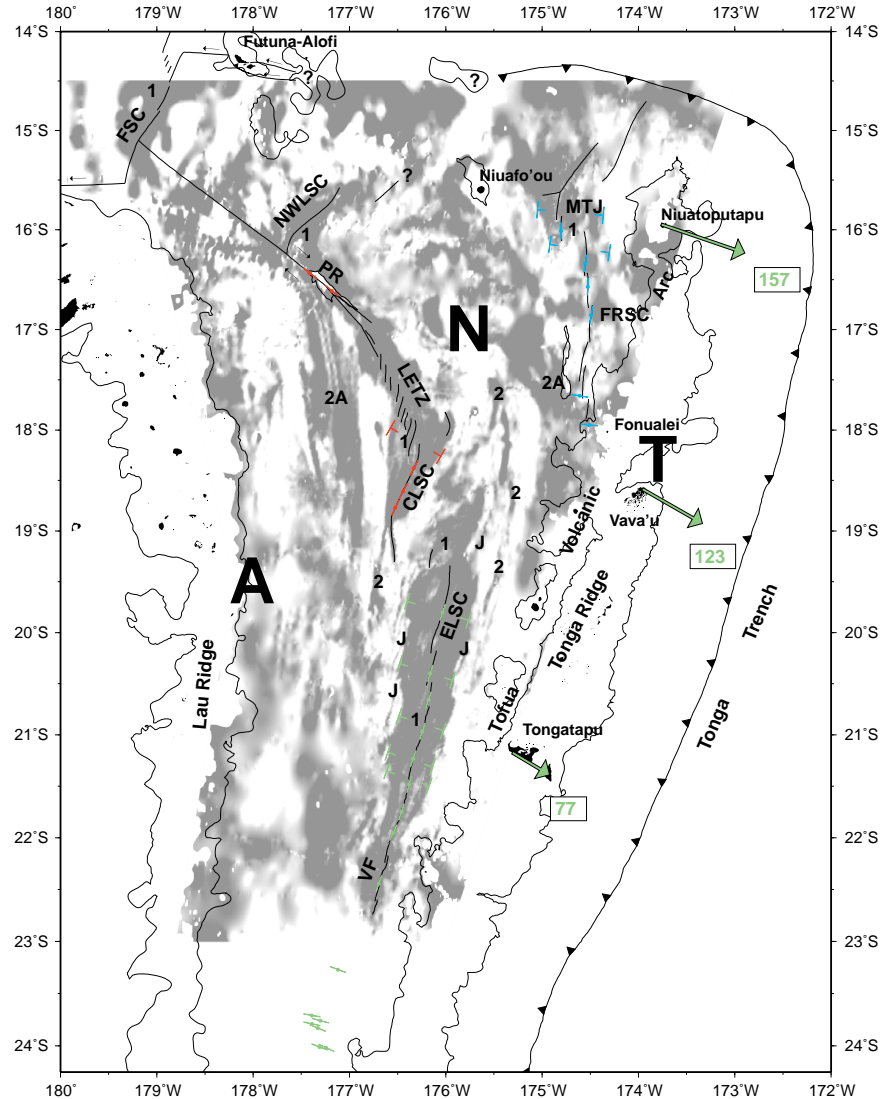


Figure 6. Lau Basin tectonic interpretation showing plate boundaries and data points used to derive the kinematic model. Gray areas indicate regions of positively magnetized crust. A 1500-m bathymetric contour outlines the Lau and Tonga Ridges and surrounds the islands (solid black) in the region. Plate boundaries are labeled as follows: CLSC, Central Lau Spreading Center; ELSC, East Lau Spreading Center; FRSC, Fonualei Rift and Spreading Center; FSC, Futuna Spreading Center; LETZ, Lau Extensional Transform Zone; PR, Peggy Ridge Transform Fault; MTJ, Mangatolu Triple Junction; NWLSC, Northwest Lau Spreading Center. The three plates discussed in this paper are labeled: A, Australian Plate; T, Tongan Plate; N, Niuafo'ou Plate. Data used to constrain the model consist of Brunhes/Matuyama boundary conjugate pairs (indicated by "T" markers), ridge azimuths, the horizontal component of earthquake slip vectors (all plotted as solid circles with lines indicating azimuth), and GPS velocities of Tonga relative to Australia (plotted as large bold arrows with a number indicating rate in mm/yr). Tables 1–3 list these data. All data points are color coded according to their associated plate boundaries or pairs: A-T, green; A-N, red; N-T, blue.

Table 1. Brunhes/Matuyama Boundary Pairs (0.78 Myr)

Longitude 1, °W	Latitude 1, °S	Longitude 2, °W	Latitude 2, °S	Plates
176.3997	19.6920	175.7630	19.8798	A-T
176.4805	20.3028	175.9311	20.4686	A-T
176.4881	20.8154	176.0271	20.9592	A-T
176.6011	21.1709	176.1398	21.3143	A-T
176.6125	21.3518	176.1739	21.4972	A-T
176.5731	17.9792	176.0514	18.2598	A-N
175.0469	15.7982	174.3655	15.8532	N-T
174.9191	16.1471	174.3022	16.2299	N-T

Table 2. GPS Relative Velocities

Longitude, °W	Latitude, °S	Velocity, mm/yr	Azimuth	α , deg*	Plates
173.7636	15.9467	157 \pm 4	109 \pm 2	19 \pm 2	A-T
173.9600	18.5853	123 \pm 4	120 \pm 2	30 \pm 2	A-T
175.3089	21.1735	77 \pm 4	121 \pm 2	31 \pm 2	A-T

*Here α is orthogonal to relative motion inferred from the data azimuth.

Table 3. Azimuth Data

Longitude, °W	Latitude, °S	Azimuth	α , deg*	Source	Plates
176.0329	19.8004	18.8	18.8	ridge	A-T
176.1623	20.4005	17.6	17.6	ridge	A-T
176.1784	20.6605	18.4	18.4	ridge	A-T
176.2446	20.9673	18.2	18.2	ridge	A-T
176.3385	21.2334	18.2	18.2	ridge	A-T
176.3818	21.4823	14.7	14.7	ridge	A-T
176.4618	21.7502	18.1	18.1	ridge	A-T
176.5451	21.9501	24.1	24.1	ridge	A-T
176.6948	22.4444	18.7	18.7	ridge	A-T
177.12	23.27	111	21	slip vector	A-T
177.39	23.71	280	10	slip vector	A-T
177.30	23.76	105	15	slip vector	A-T
177.39	23.79	282	12	slip vector	A-T
177.33	23.83	293	23	slip vector	A-T
177.24	24.02	115	25	slip vector	A-T
177.31	24.01	291	21	slip vector	A-T
176.3286	18.3759	28.1	28.1	ridge	A-N
176.4416	18.6072	27.4	27.4	ridge	A-N
176.5238	18.7694	25.3	25.3	ridge	A-N
177.4120	16.4348	128.7	38.7	transform	A-N
177.1830	16.6111	128.7	38.7	transform	A-N
174.8030	16.0108	-0.6	-0.6	ridge	N-T
174.5510	16.3359	7.9	7.9	ridge	N-T
174.5250	16.5716	2.3	2.3	ridge	N-T
174.4900	16.8533	8.5	8.5	ridge	N-T
174.61	17.66	100	10	slip vector	N-T
174.51	17.95	276	6	slip vector	N-T

*Here α is orthogonal to relative motion inferred from the data azimuth.

3.1. Peggy Ridge and the Central Lau Spreading Center

[10] The Peggy Ridge (PR) links to the Central Lau Spreading Center (CLSC) via a complex series of left-stepping, en echelon spreading segments that comprise the Lau Extensional Transform Zone (LETZ, Figure 6) [Taylor *et al.*, 1994, 1996]. PR is the only transform fault in the central Lau Basin, and it lacks significant curvature. Details of the LETZ mapped during the MW9603 cruise reveal it to be a zone of en echelon, overlapping spreading segments, cut by a strike-slip fault in the north that is at a low angle (9°) and synthetic to PR. Slip vectors determined from focal mechanisms available for this region generally do not follow the $\sim 129^\circ$ trend that is observed along the currently active right-lateral PR transform fault. They have more similar trends to the synthetic fault (138°) that may accommodate the strike-slip component of total strain that is partitioned with easterly extension on surrounding en echelon fissure ridges (characterized by high acoustic reflectivity and Brunhes magnetization, Figures 4 and 5).

[11] The morphology and trend of the CLSC [Wiedicke and Habler, 1993] varies along axis. A distinct and abrupt bend in the ridge axis at $18^\circ 57'S$ is confirmed in our bathymetry and magnetization compilations (Figures 2 and 4). North of $18^\circ 57'S$, the southward propagation of the CLSC has generated seafloor fabric trending NNE and a north trending outer pseudofault on the west that bounds crust older than magnetic anomaly 2. South of $18^\circ 57'S$, seafloor fabric trends $\sim 175^\circ$ in a narrow zone of recent volcanism with very little sediment cover. Only at the northern end of the CLSC can we determine the seafloor spreading rate, where the Brunhes-Matuyama boundaries are parallel to the seafloor fabric and inside the propagation boundaries [Taylor *et al.*, 1996] (Figure 6).

3.2. East Lau Spreading Center

[12] The southern tip of the CLSC overlaps the northern segments of the East Lau Spreading Center (ELSC, Figure 6) [Parson *et al.*, 1990]. The ELSC consists of a left-stepping series of overlapping spreading segments; the southernmost are known as the Valu Fa (VF) ridge [Morton and Sleep, 1985; Turner *et al.*, 1999]. Only on the highest-resolution swath bathymetry can the axial segmentation south of the overlapper at $20.5^\circ S$ be observed as depicted in Figure 6 (within the apparently sinuous planform of the high acoustic reflectivity, Figure 5). Our interpretation of the ridge axis location was independently confirmed by the EW9914 cruise of Harding *et al.* [2000], who studied magma lens distribution and crustal structure between $18^\circ S$ and $23^\circ S$ using along- and across-axis multichannel seismic profiles (navigated with D-GPS and colocated with Hydrosweep swath bathymetry).

[13] As the ELSC angles southward closer to the Tofua volcanic arc, the depths decrease (to ~ 1700 m, Figure 2), the axial magnetization high increases in amplitude (Figure 4), and the lavas become more arc-like [Vallier *et al.*, 1991; Pearce *et al.*, 1995]. This may explain the lack of seafloor subsidence (actual shallowing) away from the spreading axes at 19° – $21^\circ S$ where off-axis areas may formerly have been more like Valu Fa today. The area between $23^\circ 16'S$ and $24^\circ 02'S$, immediately south of the ELSC, is marked by a set of normal faulting earthquakes (Figure 6) that provide evidence for rifting ahead of the spreading tip.

[14] The Brunhes anomaly associated with the ELSC is located asymmetrically toward the east with respect to surrounding magnetic anomalies 2 (Figures 4 and 6). Apparent eastward ridge jumps are also recorded by both J anomalies sometimes being west of the Brunhes (e.g., at $19.5^\circ S$). Estimated Brunhes Chron spreading

rates along the ELSC predict a trend of northward spreading rate increase that is greater than, and not consistent with, that observed at the CLSC (see section 4.1 below). We have not estimated spreading rates on the ELSC south of 21.5°S where the width of the Brunhes anomaly significantly narrows, apparently as a result of southward ridge propagation.

3.3. Fonualei Rift and Spreading Center

[15] The Fonualei Rift and Spreading Center (FRSC) comprises the spreading centers extending south of the Mangatolu Triple Junction (MTJ, also known as the Kings Triple Junction) [Hawkins and Helu, 1986]. Details of this rift were first mapped during the MW9603 cruise, which also revealed that the western branch of the MTJ is quite short, whereas the NE branch connects via a large overrapper with a spreading segment that continues to the northern Tonga Trench (Figures 2, 5, and 6; see also Wright *et al.* [2000]). The magnetization pattern in this region (Figure 4) in conjunction with neovolcanic zones interpreted from the bathymetry and acoustic imagery (Figures 2 and 5) show that the MTJ has reoriented during the Brunhes Chron (Figure 6). South of the MTJ, the positive Brunhes and surrounding negative Matuyama anomalies can be recognized even though bathymetry and magnetics data coverage of this region is sparser than for the CLSC and ELSC (Figures 2, 3, and 4). In particular, the magnetization inversion between 16°15' and 17°S could be significantly improved by more bathymetry (and magnetics) data. Magnetic anomalies J and 2 are poorly resolved with the available data (although both J anomalies may be present west of the Brunhes as the result of a ridge jump). Detailed mapping of the FRSC south of 17°S during the MW9603 cruise reveals that the rift flanks reach <1000 m, whereas the graben floor is at an average depth of 3500 m. Earthquakes south of the

southernmost tip of the FRSC to 18°11'S exhibit normal faulting consistent with active rifting (Figure 5).

3.4. Northwest Lau Spreading Center

[16] Extending northeast from Peggy Ridge there is a region of positive magnetization and high acoustic reflectivity (Figures 4 and 5) identified as the Northwest Lau Spreading Center (NWLSC, Figure 6) [Parson and Tiffin, 1993; Tiffin, 1993]. The spreading axis is a bathymetric ridge that is flanked by abyssal hills in a 40-km-wide zone between conjugate rifted highs (Figure 2). The NWLSC has not been mapped north of 15°30'S, although a narrower spreading segment is offset from, and overlaps, it eastward (Figures 2 and 4–6). The plate boundaries in the region of left-lateral strike-slip earthquakes (Figure 5) between the recently mapped Futuna Spreading Center [Pelletier *et al.*, 2001], the northern Tonga Trench, and the NWLSC remain unsurveyed.

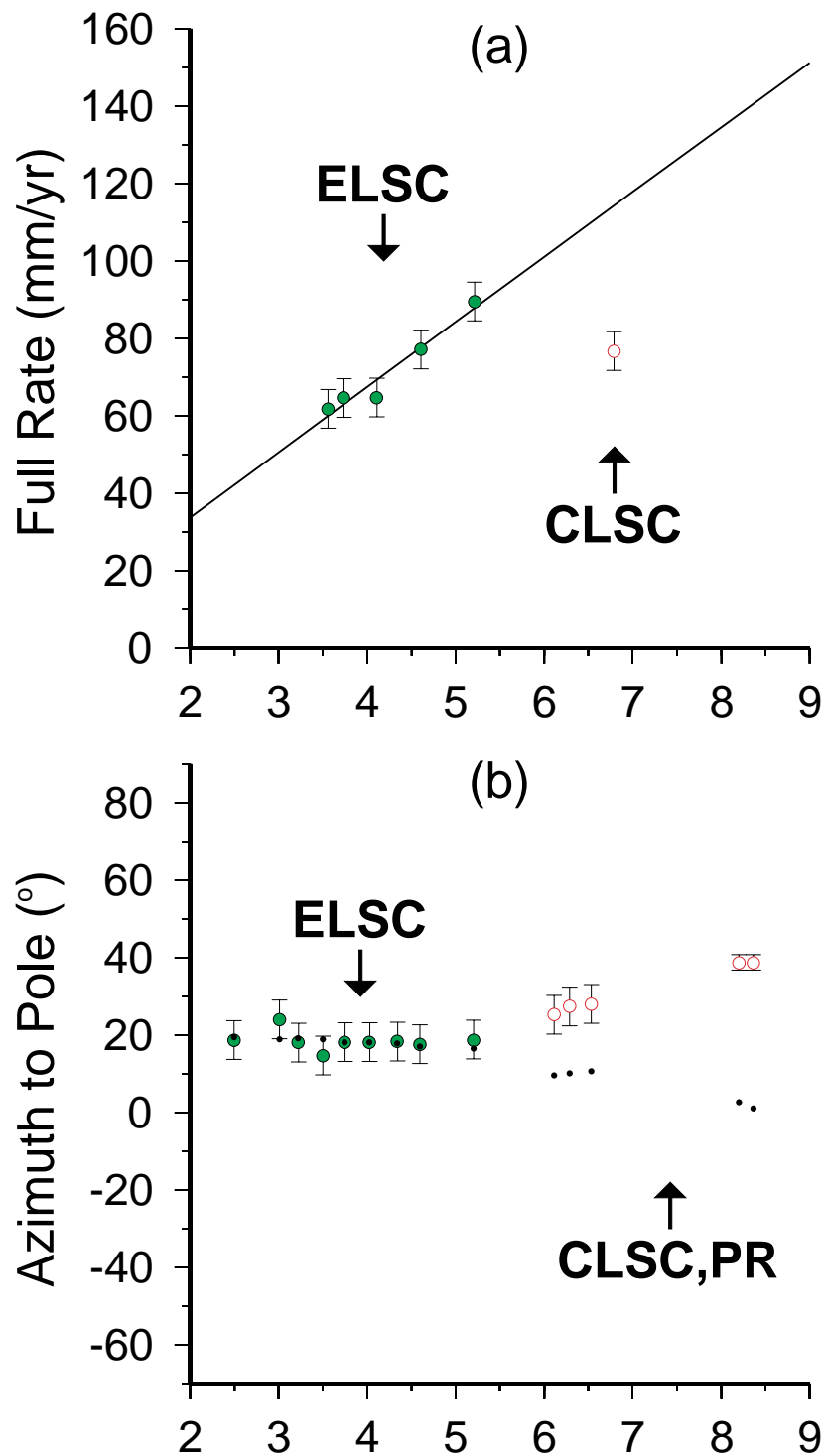
3.5. Boundaries of the Proposed Niuafu'ou Microplate

[17] There is a region between the NWLSC, the PR/LETZ/CLSC and the MTJ/FRSC that is mostly aseismic and lies south of a ~100-km-wide zone of left-lateral strike-slip earthquakes north of Niuafu'ou (Figures 5 and 6) [also see Hamburger and Isacks, 1988; Pelletier *et al.*, 1998]. We refer to this aseismic region as the Niuafu'ou (N) microplate (Figure 6). To the south of this aseismic region, a few earthquakes are recorded and located, but no distinct narrow plate boundary can be mapped between the FRSC and the CLSC or ELSC.

4. A Three-Plate Kinematic Model

4.1. Motivation

[18] The original focus of our kinematic model was simply to find the location of the Australia-Tonga pole. Working under the starting hypoth-



Angular Distance From Case 1a A-T Pole (°)

esis that the ELSC and the PR/LETZ/CLSC plate boundaries were both separating Australia and Tonga, all of the model constraints for these two boundaries were initially inverted together to determine a pole using methods described in section 5. This calculation revealed that the model constraints observed along the PR/LETZ/CLSC system did not fit well with predictions from an Australia-Tonga pole derived from the data for the ELSC system (Figure 7). We realized that motions across the ELSC and the PR/LETZ/CLSC are not copolar and that a system of more than two plates is necessary to adequately model the kinematics of the Lau Basin.

4.2. Proposed Three-Plate Model

[19] We propose that motion between the Australian (A) plate and the Tongan (T) plate is partitioned along the boundaries of the intervening Niuafu'ou (N) microplate. The tectonics of the following proposed plate boundaries are analyzed: (A-T) ELSC, (A-N) PR, LETZ, CLSC, and (N-T) FRSC. This proposition requires that an A-N-T triple junction exist somewhere between the CLSC-ELSC-FRSC.

4.3. Model Constraints

[20] The following data types are used as model constraints: (1) spreading rates (finite over 0.78 Ma), (2) GPS relative velocities, (3) the horizontal component of earthquake slip vectors, (4) transform fault azimuths, and (5) selected ridge axis azimuths (see below). The data used in our inversions are plotted in Figure 6 and listed in Tables 1–3.

[21] Table 1 presents Brunhes/Matuyama boundary pairs that were carefully picked to avoid complex areas produced by overlapping spreading centers. By studying their associated conjugate off-axis morphologies we picked these pairs of points to have been near the same location along spreading axes at 0.78 Ma. The Brunhes/Matuyama boundary pairs are directly associated with spreading rate, but, when close to Euler poles as here, the actual rates vary slightly with pole position. We estimate the spreading rate errors to be ± 5 mm/yr (i.e., one standard deviation is 5 mm/yr).

[22] Table 2 lists geodetically determined A-T opening rates and azimuths as reported by Bevis [1997]. No geodetic data are currently available for A-N or N-T motions. Errors on the geodetic data are ± 4 mm/yr in rate and $\pm 2^\circ$ in azimuth [Bevis, 1997].

[23] Table 3 lists three types of azimuthal data. Transform fault azimuths were measured along the active portion of the PR, with an estimated error of $\pm 2^\circ$. In the absence of any other transform faults along the LETZ, CLSC, ELSC, and FRSC, all of which are characterized by overlapping spreading segments, we considered alternate indicators of spreading direction. We chose to include the azimuths of ridge axes measured along central straight segments away from their overlapping tips (which excluded any measurements from the LETZ). Our rationale was that, even in areas of oblique spreading such as the Reykjanes Ridge, the centers of such sigmoidal spreading segments or axial volcanic ridges are predominantly orthogonal to the spreading direction

Figure 7. Comparison of (a) measured rates and (b) azimuths (in colored symbols) versus modeled values (in black) predicted by the case 1a A-T pole (refer to Table 4 and section 4.1). The data along the PR/LETZ/CLSC (open symbols) are not predicted by a pole describing the data along the ELSC (solid symbols). We infer that the motions across these two boundaries are not copolar, i.e., a system of at least three plates is needed to adequately describe the kinematics of the Lau Basin.

[Murton and Parson, 1993; Taylor *et al.*, 1994]. From these global considerations we assigned errors of $\pm 5^\circ$ to the local ridge azimuths in terms of their fidelity as measures of the orthogonal to the spreading direction. We also considered the focal mechanisms of earthquakes. As discussed in section 3.1 above, we interpret the strike-slip earthquakes along the PR-LETZ-CLSC to record only a component of the full plate motion, so we did not include their slip vectors in our inversions. We did, however, include the horizontal component of earthquake slip vectors from normal faults associated with rifting south of the ELSC and FRSC, but only from those earthquakes with nearly pure dip-slip solutions (rakes within $\pm 20^\circ$ of -90°). To choose between the two possible slip vectors, we first determined Euler poles without using slip vector information and then chose the slip vector for each earthquake that was most consistent with the slip predicted by those poles. Given the errors inherent in CMT focal mechanism solutions and teleseismic earthquake location, we estimate errors of $\pm 10^\circ$ for the earthquake slip data.

5. Methodology

5.1. General Procedure

[24] To test whether (1) modern geodetic and earthquake motions are descriptive for the last 780,000 years and (2) Euler poles can be located that fit the data along each of the plate boundaries and also meet three-plate closure criterion, we inverted the data in stages. To test point 1 above, in the first case we used only the model constraints from the marine geophysical data. We then compared the predictions of these poles with the geodetic and earthquake slip data that had been omitted. As will be shown, the data were found to be compatible, so we then incorporated all the data together in the second case. To test point 2 above, for each of the two cases we first derived the best fit Euler poles

(and their 95% confidence regions) for each of the three plate boundaries. We then simultaneously searched the three confidence regions to determine if a common solution of three poles can be found that matches all the data constraints as well as the following three-plate closure criterion:

$${}_A\omega_T = {}_A\omega_N + {}_N\omega_T, \quad (1)$$

where ${}_A\omega_T$ refers to the vector describing the motion of plate T relative to plate A and is specified by a latitude, longitude, and angular rate of rotation (ω). This procedure produced four inversions that we will refer to as case 1 (a and b) and case 2 (a and b).

5.2. Inverting the Data

[25] For both cases a grid search was conducted to find the poles of opening that statistically best fit the model constraints for motions between each of the three pairs of plates. An initial latitude-longitude grid search at 0.5° was refined to 0.1° at the same time as the angular rate of opening, ω , was refined from an initial “best guess” value to a resolution of $0.1^\circ/\text{Myr}$. Chi-squared statistics were calculated for each grid node (the sums of [squares of {observation minus prediction}] divided by the square of the standard deviation of the observation). The best fitting Euler pole for a given boundary was determined by the latitude-longitude grid node (and associated ω value) that carried the lowest chi-square statistic. We then used a bootstrap method (refer to section 5.3) to generate 95% confidence regions about each of these poles. Finally, poles within the three confidence regions that result from the bootstrap analysis were simultaneously searched to find the best fitting set of poles that also met the three-plate closure criterion (equation (1)).

5.3. Confidence Regions

[26] Several methods have been proposed and analyzed for determining the effect of disparate



Table 4. Case 1a Pole Solutions

Pole	Boundary	Longitude, °W	Latitude, °S	ω , deg/Myr
A-T	ELSC	177.6	24.8	8.7
A-N	CLSC,PR	171.5	9.6	4.3
N-T	FRSC	174.9	20.0	11.5

data types and errors on calculated poles of opening [Wilson, 1993]. The method used here is based on bootstrap resampling [Efron and Tibshirani, 1986], in which data inputs are randomly resampled such that some data values

are selected multiple times while others are left out. For each of 1000 of these “resampled” data sets, calculations were completed using the methods described in section 5.2. This bootstrap process generated 1000 points scattered

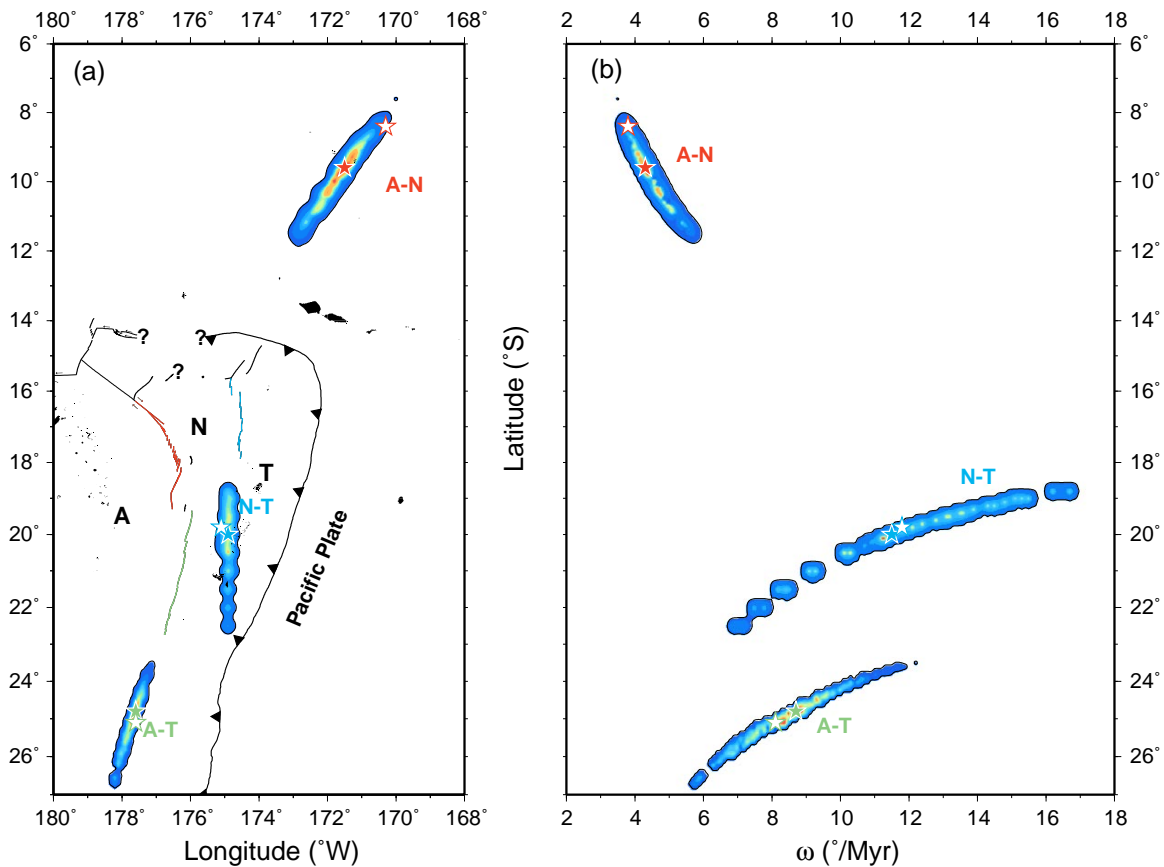
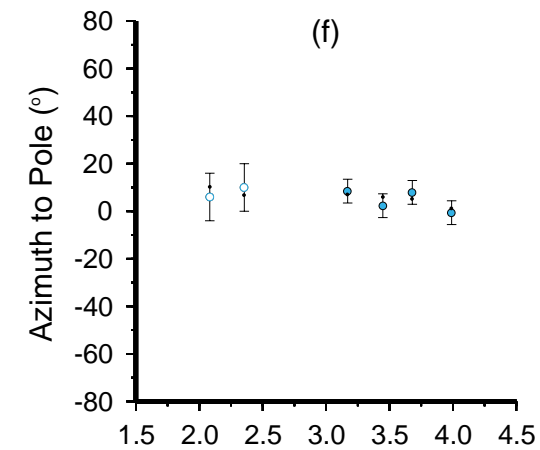
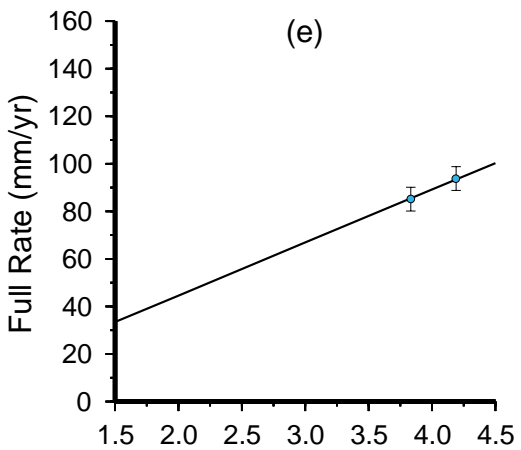
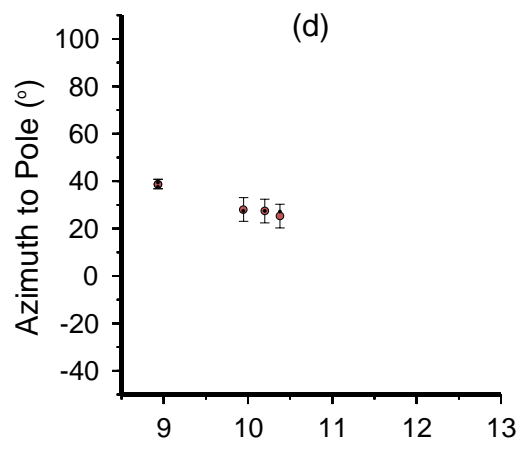
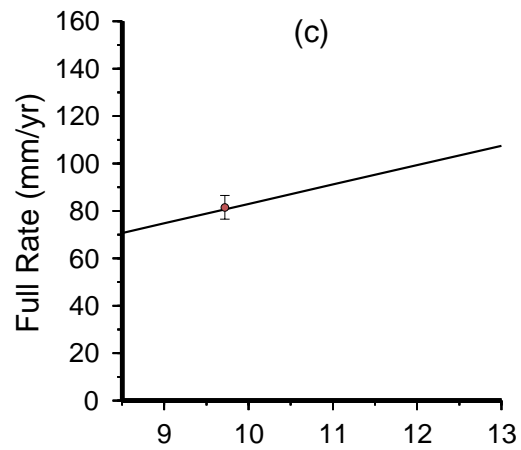
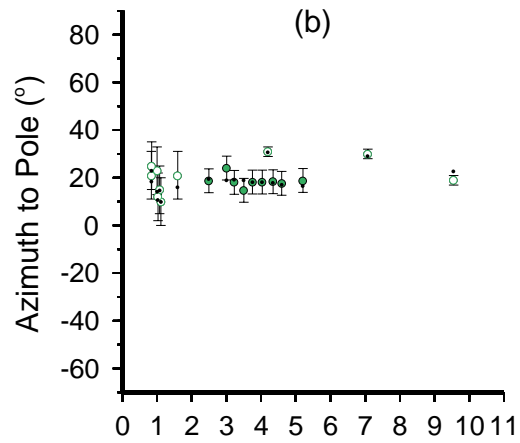
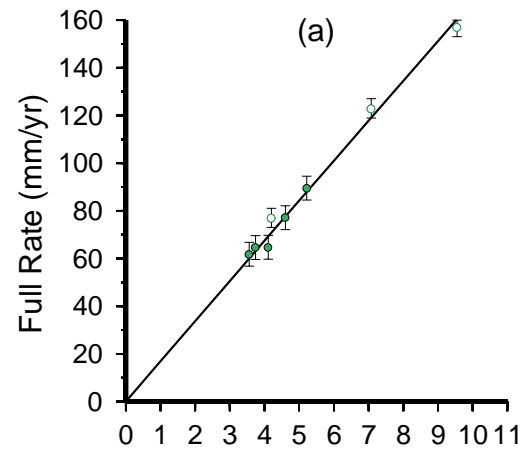
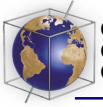


Figure 8. Euler poles and 95% confidence regions determined from the spreading rate, transform, and ridge azimuth data (i.e., independent of the earthquake and GPS data). Solid stars show the locations of the case 1a pole solutions that best fit the data for each plate pair (refer to Table 4); open stars show the locations of the case 1b pole solutions, which also meet the three-plate closure criterion (refer to Table 5). Plate boundaries are color coded as in Figure 6. (a) Confidence regions on latitude-longitude projection. (b) Confidence regions on latitude- ω projection (ω is the angular rate).



Angular Distance From Case 1a Poles (°)
A-T (a, b); A-N (c, d); N-T (e, f)



Table 5. Case 1b Pole Solutions

Pole	Boundary	Longitude, °W	Latitude, °S	ω , deg/Myr
A-T	ELSC	177.6	25.1	8.1
A-N	CLSC,PR	170.3	8.4	3.8
N-T	FRSC	175.1	19.8	11.8

about each best fit pole solution to represent a reasonable indication of the possible pole error. Contours of confidence limits were generated about the best fitting pole using a density function and methods described by *Wilson* [1993]. The use of a density function allows for 95% confidence regions to be simultaneously derived for all three-pole parameters (latitude, longitude, and ω).

6. Results

6.1. Case 1a

[27] Table 4 lists the best fitting Euler poles determined from the spreading rate, transform, and ridge azimuth data along each boundary between the three pairs of plates. The locations of these case 1a poles are plotted as solid stars in Figure 8 along with their associated 95% confidence regions. Figure 8a shows the error regions in latitude-longitude space, and Figure 8b shows the error regions in longitude-omega space. Figure 9 shows that the rates and azimuths calculated from the poles listed in Table 4 generally match the observations to within their estimated errors.

[28] The error regions of the three poles are not very tightly constrained (Figure 8) in part because the inverted data exist for only a small range of angular distances ($\sim 2^\circ$, Figure 9). The error regions for both the A-T and N-T poles

span a wide range of possible omega values because close proximity of the poles to their respective plate boundaries means that a small change spatially results in a large change in angular rate.

6.2. Case 1b

[29] The best fitting set of poles for the marine geophysical data that also meet the three-plate closure criterion (equation (1)) are listed in Table 5 and plotted as open stars in Figure 8. The fact that this set of case 1b poles can be defined within the 95% confidence regions of the case 1a poles is significant. It means that relative motions that meet the closure criterion may be realized for the Tongan forearc plate, the Niuafu'ou microplate, and the large Australian Plate system for periods of at least 0.78 Myr (but see section 6.4 below).

6.3. Compatibility Between the Geodetic, Earthquake, and Marine Data

[30] We compared the predictions of the case 1a poles with the geodetic and earthquake slip data (that had been omitted in the first data inversion) to test whether the marine geophysical and modern data sets are compatible along the relevant plate boundaries. The results are plotted in Figure 9. Plate velocities predicted from the marine geophysical data match the A-T geodetic velocities of *Bevis* [1997] to within one or two standard errors (Figures 9a and 9b).

Figure 9. Comparison plots of (a, c, e) spreading rate and (b, d, f) azimuth data (color coded as in Figure 6) versus modeled values (in black) predicted by the case 1a poles (Table 4) as a function of angular distance from the poles. Comparison with earthquake and GPS data (open symbols) not used to derive the case 1a poles shows all the data are compatible within one or two standard errors.

**Table 6.** Case 2a Pole Solutions

Pole	Boundary	Longitude, °W	Latitude, °S	ω , deg/Myr
A-T	ELSC	177.7	25.0	8.4
A-N	CLSC,PR	171.5	9.6	4.3
N-T	FRSC	174.9	20.1	11.2

Thus any discrepancies of the geodetic relative plate velocity values (as revised by *Bevis* [1997]) with those independently determined by marine magnetic data are much less than the ~25% reported by *Bevis et al.* [1995] and *Taylor et al.* [1996]. The horizontal component of the earthquake slip vectors are within error of their predicted values. These comparisons indicate that all the data are sufficiently compatible to be included in a single inversion (case 2).

6.4. Case 2

[31] The results of including the geodetic and earthquake data with the marine geophysical data (case 2a for the three pairs of plates and case 2b in which the poles also meet the three-plate closure criterion) are reported in Tables 6 and 7 and plotted in Figure 10 as closed and open stars, respectively. The case 2 poles are similar to the case 1 poles with two exceptions. The A-T 95% confidence region shrinks significantly because of (1) the increased range of angular distances and azimuths in the full data set and (2) the strict match to the geodetic vectors required for each trial pole, i.e., unlike the Brunhes boundary pairs, the geodetic vectors are unaffected by the spatial location of the poles being tested statistically. In contrast, the N-T 95% confidence region expands as a result of adding the two earthquake slip vectors to the data set.

[32] The data compatibility plots of Figure 11 show that nearly all the predictions of the Case 2a poles remain within the error of the observations. In contrast, the data compatibility plots for Case 2b (Figure 12) show that the compromise required to complete the plate circuit forces several predicted azimuth values for the N-T pole slightly outside one standard error of the observations. This and the fact that the A-N and N-T poles for case 2b lie near the edge of the 95% confidence regions for case 2a (Figure 10) suggests that the poles describing the motions of the Niuafu'ou microplate relative to Australia and Tonga may have changed slightly within the last 0.78 Myr. Such an evolution might be expected given that both the CLSC and FRSC are propagating southward and that the FRSC has reoriented within the Brunhes chron; however, this inference is at the limit of resolution of the available data.

6.5. Compilation of Results

[33] The results of our three-plate kinematic model of Lau Basin opening are summarized in Figure 13. Observed full spreading rate values are a function of the spatial location of the pole and the picked pairs of Brunhes/Matuyama boundary points. These values are included in Figure 13 and correspond to the values plotted in Figure 12. The resultant small

Table 7. Case 2b Pole Solutions

Pole	Boundary	Longitude, °W	Latitude, °S	ω , deg/Myr
A-T	ELSC	177.7	25.0	8.4
A-N	CLSC,PR	170.2	8.2	3.8
N-T	FRSC	175.2	19.8	12.1

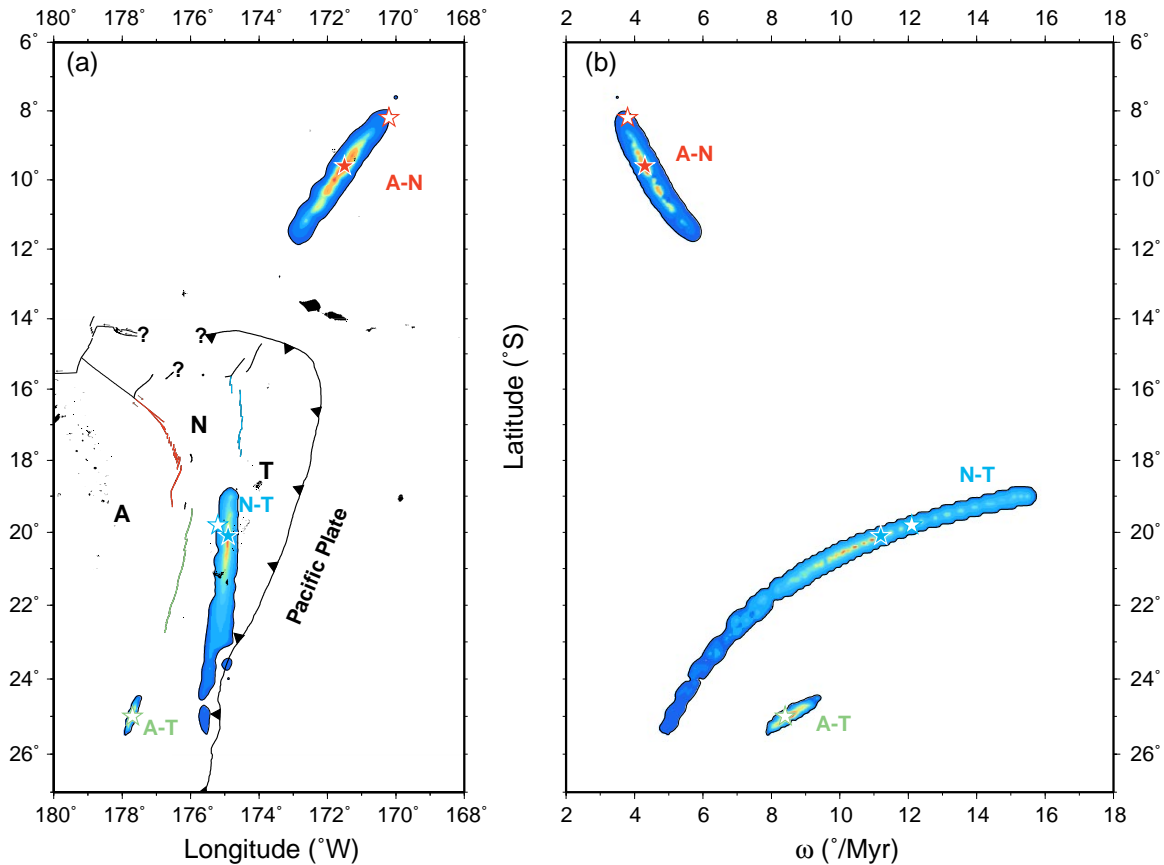


Figure 10. Euler poles and 95% confidence regions determined from all the data (Tables 1–3). Solid stars show the locations of the case 2a pole solutions (refer to Table 6); open stars show the locations of the case 2b pole solutions (refer to Table 7). Plate boundaries and Euler poles are color coded as in Figure 6. (a) Confidence regions for latitude-longitude projection. (b) Confidence regions for latitude- ω projection (ω is the angular rate).

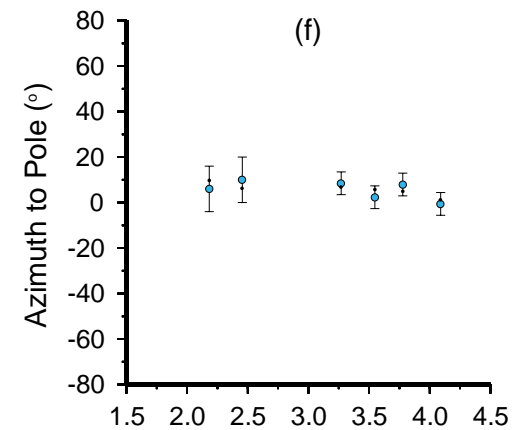
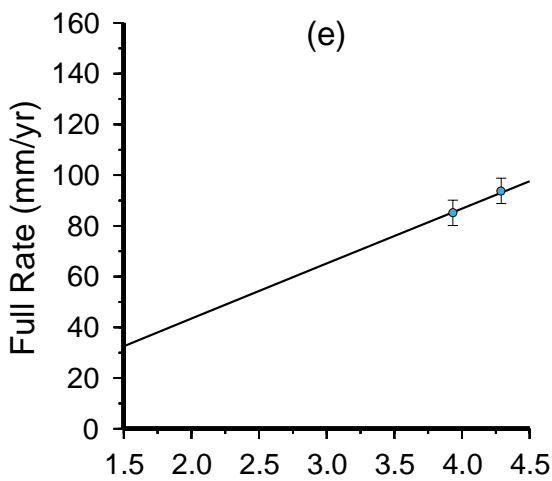
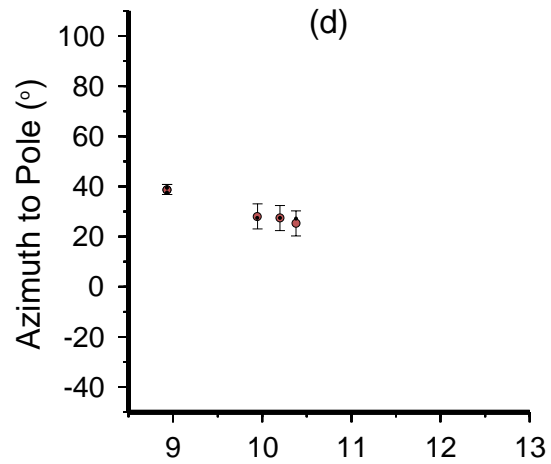
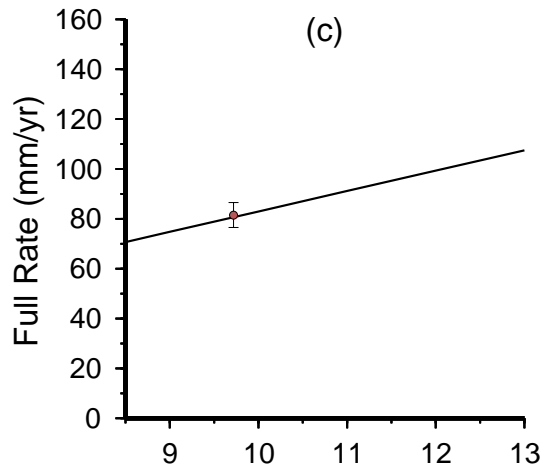
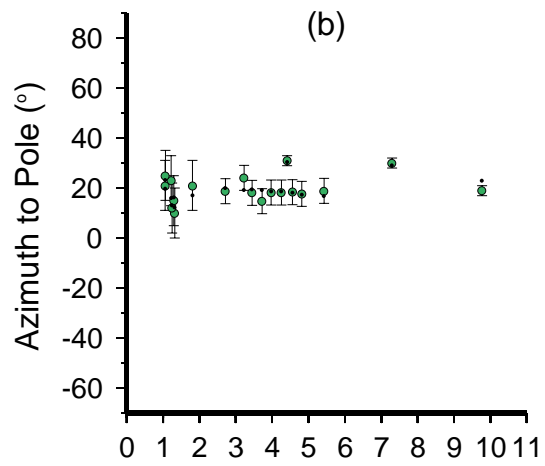
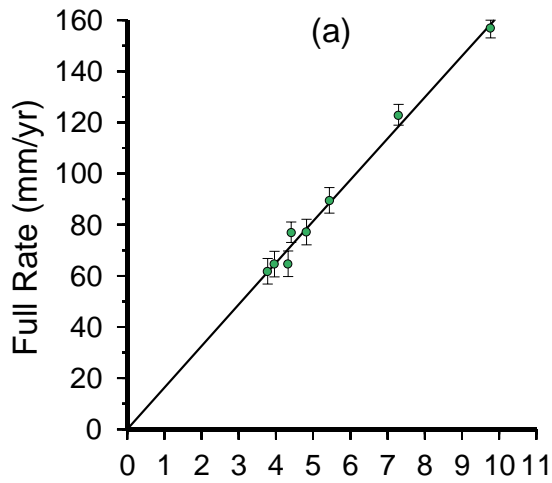
circles subtended between the chosen Brunhes/Matuyama boundaries and their respective case 2b pole solution are also plotted. The closer the pole is to the boundary, the greater the curvature in the subtended small circle.

7. Discussion

7.1. Comments on the Three-Plate Model

[34] Our three-plate model accounts for the primary kinematics of Lau Basin opening, including that of the newly defined FRSC plate

boundary and the Niufo'ou microplate. Our kinematic analysis confirms that spreading on the CLSC and ELSC are not copolar and is consistent with the normal faulting earthquakes near 24°S being rifting events close to the A-T pole. We have not modeled the back arc basin region north of ~15.5°S because of the paucity of geophysical data there. Nevertheless, it is clear from the existing data that additional microplates and/or deformation zones are present in this northern borderland region of strike-slip seismicity (Figure 13) [Pelletier *et al.*, 2001].



Angular Distance From Case 2a Poles (°)
A-T (a, b); A-N (c, d); N-T (e, f)

[35] A classical narrow southern boundary has not been identified for the proposed Niufo'ou microplate (see section 7.2). However, the microplate clearly is disparate enough from the Australian and Tongan plates to be kinematically modeled using constraints at the boundaries that could be identified. In fact, one of the main results of our analysis is that the kinematics of three plate-scale regions in the Lau Basin can be described, even given the ambiguity of the southern boundary of the Niufo'ou microplate and the A-N-T triple junction.

[36] A majority of the geophysical constraints used as inputs are well matched by the three-plate kinematic model and the resultant case 2 pole solutions are compatible to within one or two standard errors of the observed A-T geodetic vectors. That the geodetic vectors are compatible with the marine-magnetic-determined spreading rates implies that the A-T plate motion vectors determined geodetically are applicable since at least 0.78 Ma. This is a robust conclusion for the A-T pole and data, independent of the three-plate model and the interpretation of data on the other plate boundaries. That is, the A-T marine, earthquake, and geodetic data are all compatible within one, rarely two, standard errors. They jointly define the best constrained Euler pole (25°S, 177.7°W, 8.4°/m.y.) which is the same for case 2a and case 2b and almost identical for case 1.

7.2. Nature of Plate Boundaries

[37] Although the three-plate model accounts for a majority of the tectonic features throughout the Lau Basin, some of the boundaries in the A-N-T system cannot be fully understood within the scope of this kinematic model. The LETZ, for example, is a complex set of over-

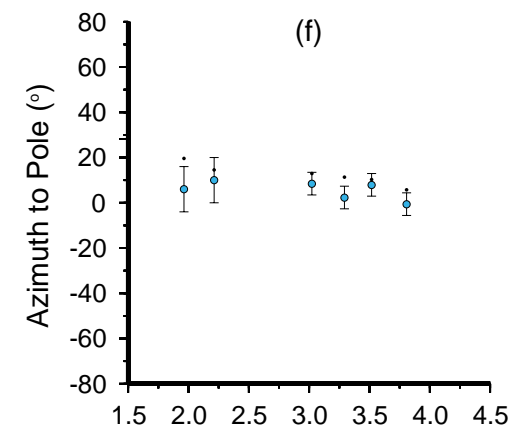
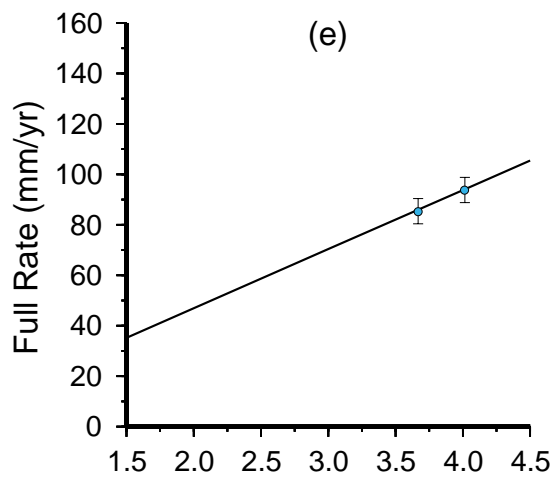
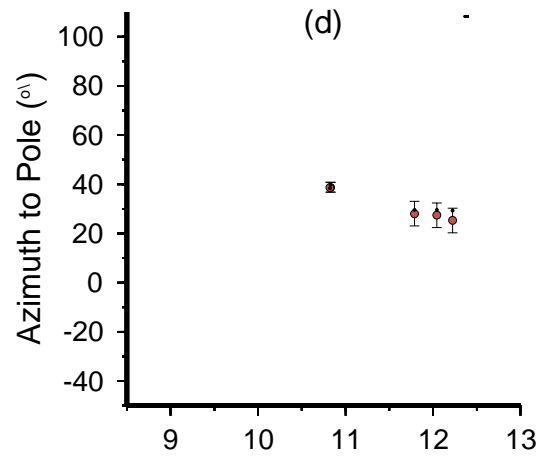
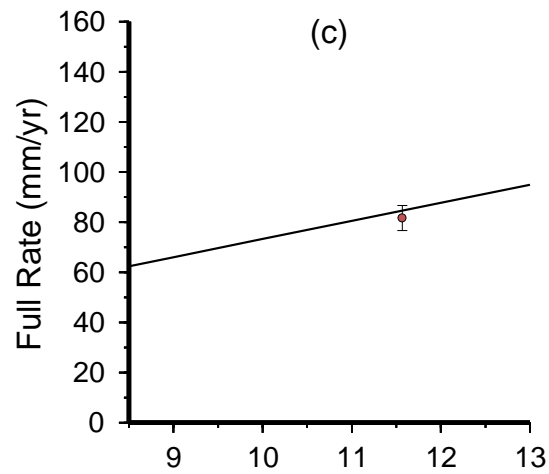
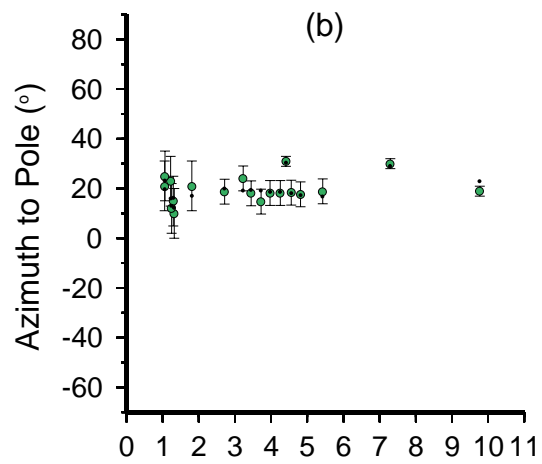
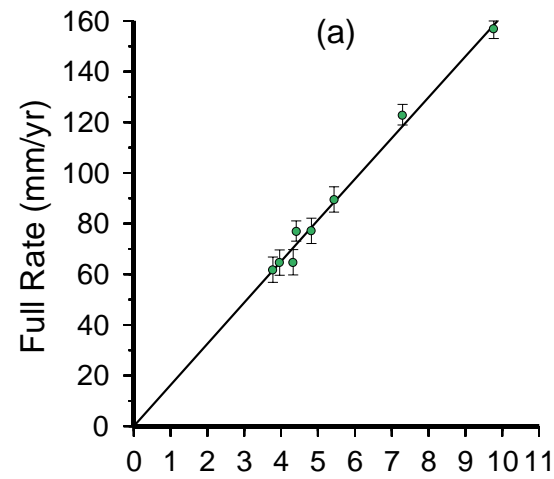
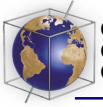
lapping ridges that accommodate both extensional and strike-slip motion. Brunhes-age lavas have overprinted Matuyama-age crust within this region.

[38] Most notably, the southern boundary of the Niufo'ou microplate has not been identified despite full swath mapping. The only evidence of a boundary is the set of scattered seismicity (including a $M_w = 6.5$ event) between the southern tip of the FRSC and the ELSC (Figures 5 and 13). Therefore, although the kinematics for the microplate can be defined, there may be migrating and/or diffuse plate boundaries that are not accounted for in our model. A similar situation exists in the Pacific-Nazca-Cocos triple junction region where the boundaries of the Galapagos microplate are not fully identifiable [Lonsdale, 1988]. Nevertheless, using the case 2b solution of the N-T pole, we can estimate the relative motions between the microplate and the Tongan plate in the vicinity of their inferred boundary zone. Near the southern tip of the FRSC, N-T rates of relative motion are predicted to be ~ 47 mm/yr (± 5 mm/yr) decreasing to ~ 20 mm/yr (± 5 mm/yr) at the northern tip of the ELSC. The boundary between the FRSC tip and ELSC may be rapidly migrating, as is that between the CLSC and ELSC, in which case a narrow plate boundary would not necessarily be evident. Note that our three-plate model also calls into question the use of the CLSC-ELSC region as a simple example of bookshelf tectonics within a large propagating overlayer [Wetzel *et al.*, 1993].

7.3. Propagation Rates at the CLSC

[39] We can quantify the rates of both the CLSC propagation and the rates of rapid extension

Figure 11. Comparison of (a, c, e) rate and (b, d, f) azimuth data (colored) versus modeled values (in black) predicted by the case 2a poles (Table 6) that invert all the data.



Angular Distance From Case 2b Poles (°)
A-T (a, b); A-N (c, d); N-T (e, f)

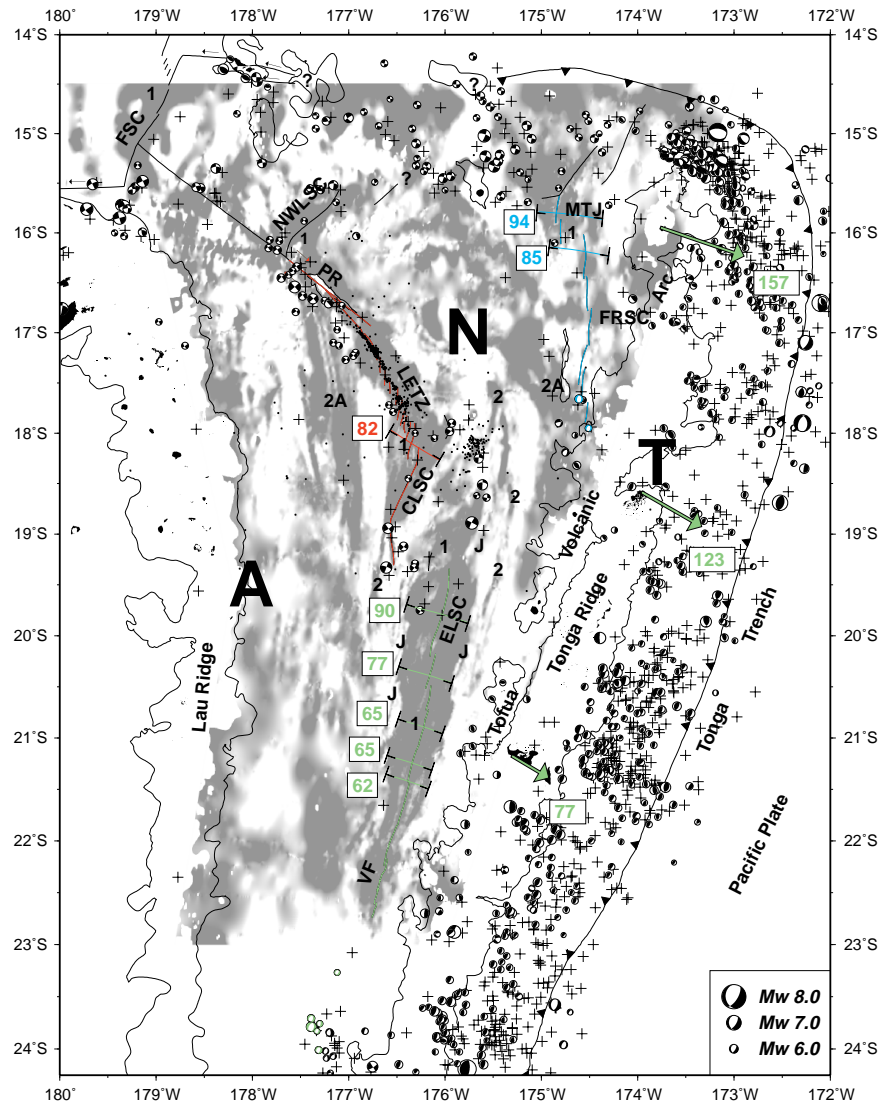


Figure 13. Lau Basin tectonic and kinematic interpretation. To the plate boundary and positive magnetization base map of Figure 5 are added the seismicity data of Figure 4 and the results from the three-plate kinematic model of case 2b (Table 7). Plate boundaries, focal mechanisms used in case 2, and small circles (subtended about each of the respective poles) plotted between Brunhes/Matuyama boundary conjugate pairs (indicated by “T” markers), are colored according to their respective pole (A-T, green; A-N, red; N-T, blue). Measured spreading rates and GPS velocities of T relative to A are labeled in mm/yr (within boxes).

to the tectonic tip by calculating synthetic Brunhes/Matuyama boundaries using the case 2b A-N pole. The ratio of the distance between

the propagation boundaries relative to the distance across the synthetic Brunhes/Matuyama boundaries gives the age of the propagation

Figure 12. Comparison of (a, c, e) rate and (b, d, f) azimuth data (colored) versus modeled values (in black) predicted by the case 2b poles (Table 7) that invert all the data and meet the three-plate closure criterion.

boundary as a percentage of 780,000 years. Using the angular rate and position associated with the case 2b A-N pole, we estimate that the age of the propagation boundary at 18°57'S (Figure 13) is ~145,000 yrs, which in turn implies a propagation rate of 120 mm/yr along the CLSC. The distance from 18°57'S to the tectonic tip (located at the southern terminus of the CLSC) is ~46 km, which implies a very rapid propagation rate of 320 mm/yr for this segment.

7.4. Implications for Regional Tectonics

[40] South of the Lau Basin lies the Havre Trough and the Taupo Rift (Figure 1), a region known to be actively extending [Parson and Wright, 1996]. Because the A-T pole is located near 25°S within the bathymetric saddle separating the Lau Basin and Havre Trough (Figure 1), it predicts compression farther south. This observation implies that the extension in the Havre Trough and Taupo Rift is not copolar with the Lau Basin opening as described by the A-T pole; i.e., that the Tonga Ridge is rotating away from the Lau Ridge faster than an extrapolation of Havre Trough opening rates would imply (Figure 1).

[41] In addition, geodetically determined rates of Pacific-Tonga motion range from 150 mm/yr at 21°S to 240 mm/yr at 16°S [Bevis, 1997]. We have shown that the three-plate kinematic model for Lau Basin opening, and particularly the A-T Euler pole and rates, are compatible (within one or two standard errors) to the geodetically determined A-T plate velocities. We conclude that subduction of the Pacific Plate at the Tonga Trench has been at these fast rates for at least 0.78 Ma.

8. Conclusions

[42] 1. Motions across the ELSC and the PR/LETZ/CLSC plate boundaries are not copolar.

We define a three-plate system (A-N-T) whose kinematics statistically match Lau Basin (1) Brunhes spreading rates, (2) spreading center and transform fault azimuths, (3) earthquake focal mechanism slip vectors, and (4) geodetically determined A-T velocities.

[43] 2. Seafloor spreading rates and azimuths of the ELSC, and earthquake slip vectors of rifting events, are compatible (within one or two standard errors) with the geodetically determined A-T velocities of Bevis [1997]. By extension, the geodetically determined Pacific-Tonga rates of subduction (240 mm/yr at 16°S [Bevis, 1997]) are applicable for at least 0.78 Myr. During this time the angular rate of opening of the Lau Basin has been faster than that of the Havre Trough.

[44] 3. Rates of southward propagation of the CLSC to 18°57'S are estimated at 120 mm/yr according to our case 2b A-N pole. South of 18°57'S, the tectonic tip has rapidly migrated south at a rate similarly estimated to be 320 mm/yr.

[45] 4. The newly recognized Niuafu'ou microplate lacks a well-defined plate boundary on its southern border, which may be migrating southward with the propagating CLSC and its overlap zone with the ELSC. Nevertheless, teleseismic earthquakes have not been recorded in the interior of the microplate, which is compatible with our three-plate kinematic model in which A-T motion from 15.5°S to 19°S is partitioned between A-N motion on PR/LETZ/CLSC and N-T motion on the FRSC. Additional microplates and/or deformation zones are present in a borderland region of strike-slip seismicity further north.

[46] 5. The poles describing the motions of the Niuafu'ou microplate relative to Australia and Tonga may have changed slightly within the last 0.78 Myr, as might be expected given that

both the CLSC and FRSC are propagating southward and that the FRSC has reoriented within the Brunhes chron.

Acknowledgments

[47] The geophysical data compilation required as the basis for this kinematic analysis would not have been possible without the generous contributions, often prior to other publication, of numerous individuals and institutions including the following: Michael Bevis, Sherman Bloomer, Toshiya Fujiwara, Andrew Goodliffe, Alistair Harding, John Hughes Clarke, Graham Kent, Fernando Martinez, Lindsay Parson, Christine Peirce, David Phillips, Etienne Ruellan, Martin Sinha, Dawn Wright, Toshitsugu Yamezaki, Metal Mining Agency of Japan, and the South Pacific Applied Geoscience Commission. Andrew Goodliffe merged the acoustic reflectivity data reproduced in Figure 5. Fernando Martinez, Andrew Goodliffe, and Steve Martel provided insightful advice throughout this project. Constructive reviews by Lindsay Parson, Dan Scheirer (in particular), and Don Forsyth (the Associate Editor) significantly improved the final manuscript. This work was supported by a grant from the National Science Foundation.

References

- Bevis, M., Geodetic measurements in the Tonga-Lau arc system (abstract), *Eos Trans. AGU*, 78, 697–698, 1997.
- Bevis, M., F. W. Taylor, B. E. Schutz, J. Recy, B. L. Isacks, S. Hely, R. Singh, E. Kendrick, J. Stowell, B. Taylor, and S. Calmant, Geodetic observations of very rapid convergence and back-arc extension at the Tonga arc, *Nature*, 374, 249–251, 1995.
- Caress D. W., and Chayes D. N. New software for processing sidescan data from sidescan-capable multibeam sonars, *Proc. IEEE Oceans 95 Conf.*, 997–1000, 1995.
- Chase, C. G., Tectonic history of the Fiji Plateau, *Geol. Soc. Am. Bull.*, 82, 3087–3110, 1971.
- Defense Mapping Agency Hydrographic/Topographic Center, Tonga Islands DMA Chart 83560, Washington D. C., 1990a.
- Defense Mapping Agency Hydrographic/Topographic Center, Fiji-Iles de Horne DMA, Chart 83034, Washington, D. C., 1990b.
- Efron, B., and R. Tibshirani, Bootstrap methods for standard errors, confidence intervals, and other measures of statistical accuracy, *Stat. Sci.*, 1, 54–77, 1986.
- Eguchi, T., Microearthquakes and tectonics in an active back-arc basin: The Lau Basin, *Phys. Earth Planet. Inter.*, 56, 210–229, 1987.
- Fujiwara, T., T. Yamazaki, and M. Joshima, Bathymetry and magnetic anomaly of the Havre Trough and southern Lau Basin: From rifting to spreading in back-arc basins, *Earth Planet. Sci. Lett.*, 185, 253–264, 2001.
- Hamburger, M. W., and B. L. Isacks, Diffuse back-arc deformation in the southwestern Pacific, *Nature*, 332, 599–604, 1988.
- Harding, A. J., G. M. Kent, and J. A. Collins, Initial results from a multichannel seismic survey of the Lau back-arc basin (abstract), *Eos Trans. AGU*, 81, F1115, 2000.
- Hawkins, J. W., and S. Helu, Polymetallic sulphide deposit from “black smoker” chimney: Lau Basin, *Eos Trans. AGU*, 67, 378, 1986.
- Hill, P. J., and D. L. Tiffin, Geology, sediment patterns, and widespread deformation on the sea floor off Western Samoa revealed by wide-swath imagery, *Geo Mar Lett.*, 13, 116–125, 1993.
- Hughes Clarke, J. E., P. Jarvis, D. Tiffin, R. Price, and L. Kroenke, Tectonic activity and plate boundaries along the northern flank of the Fiji Platform, *Geo-Mar. Lett.*, 13, 98–106, 1993.
- Isacks, B., J. Oliver, and L. R. Sykes, Seismology and the new global tectonics, *J. Geophys. Res.*, 73, 5855–5899, 1968.
- Karig, D., Ridges and basins of the Tonga-Kermadec Island arc system, *J. Geophys. Res.*, 75, 239–254, 1970.
- Lawver, L. A., and J. W. Hawkins, Diffuse magnetic anomalies in the marginal basins: Their possible tectonic and petrologic significance, *Tectonophysics*, 45, 323–339, 1978.
- Lawver, L. A., J. W. Hawkins, and J. G. Sclater, Magnetic anomalies and crustal dilation in the Lau Basin, *Earth Planet. Sci. Lett.*, 33, 27–35, 1976.
- Lonsdale, P., Structural pattern of the Galapagos Microplate and evolution of the Galapagos Triple Junctions, *J. Geophys. Res.*, 93, 13,551–13,574, 1988.
- Macdonald, K. C., S. P. Miller, S. P. Heustis, and F. N. Spiess, Three-dimensional modeling of a magnetic reversal boundary from inversion of Deep-Tow measurements, *J. Geophys. Res.*, 85, 3670–3680, 1980.
- Martinez, F., P. Fryer, N. A. Baker, and T. Yamazaki, Evolution of backarc rifting: Mariana Trough, 20°–24°N, *J. Geophys. Res.*, 100, 3807–3927, 1995.
- Morton, J. L., and N. H. Sleep, Seismic reflections from a Lau Basin magma chamber, in *Geology and Offshore Resources of Pacific Island Arcs-Tonga Region*, edited by D. Scholl and T. Vallier, pp. 441–453, Circum-Pacific Council for Energy and Mineral Resour., Houston, Tex., 1985.
- Murton, B. J., and L. M. Parson, Segmentation, volcanism and deformation of oblique spreading centres: A quantitative study of the Reykjanes Ridge, *Tectonophysics*, 222, 237–257, 1993.

- Parker, R. L., The rapid calculation of potential anomalies, *Geophys. J. R. Astron. Soc.*, **31**, 447–455, 1972.
- Parker, R. L., and S. P. Heustis, The inversion of magnetic anomalies in the presence of topography, *J. Geophys. Res.*, **79**, 1587–1593, 1974.
- Parson, L. M., and J. W. Hawkins, Two-stage ridge propagation and the geological history of the Lau backarc basin, *Proc. Ocean Drill. Program Sci. Results*, **135**, 819–828, 1994.
- Parson, L. M., and D. L. Tiffin, Northern Lau Basin: Backarc extension at the leading edge of the Indo-Australian Plate, *Geo Mar Lett.*, **13**, 107–115, 1993.
- Parson, L. M., and I. C. Wright, The Lau-Havre-Taupo back-arc basin: A southward propagating, multi-stage evolution from rifting to spreading, *Tectonophysics*, **263**, 1–22, 1996.
- Parson, L. M., J. A. Pearce, B. J. Murton, and R. A. Hodkinson, and the RRS *Charles Darwin* Scientific Party, Role of ridge jumps and ridge propagation in the tectonic evolution of the Lau back-arc basin, southwest Pacific, *Geology*, **18**, 470–473, 1990.
- Parson, L. M., J. W. Hawkins, and P. M. Hunter, Morphotectonics of the Lau Basin Seafloor — Implications for the opening history of backarc Basins, *Proc. Ocean Drill. Program Initial Rep.*, **135**, 81–82, 1992.
- Pearce, J. A., M. Ernewein, S. H. Bloomer, L. M. Parson, B. J. Murton, and L. E. Johnson, Geochemistry of Lau Basin volcanic rocks: Influence of ridge segmentation and arc proximity, in *Volcanism Associated with Extension at Consuming Plate Margins*, edited by J. L. Smellie, *Geol. Soc. Spec. Publ.*, **81**, 53–75, 1995.
- Pelletier, B., S. Calmant, and R. Pillet, Current tectonics of the Tonga-New Hebrides region, *Earth Planet Sci Lett.*, **164**, 263–276, 1998.
- Pelletier, B., Y. Lagabriele, M. Benoît, G. Cabioch, S. Calmant, E. Garel, C. Guivel, and J. Perrier, Newly discovered active spreading centers along the North Fiji Transform Zone (Pacific-Australia Plates Boundary): Preliminary results of the R/V *l'Atalante* ALAUF1 cruise (February–March 2000), *Ridge Events*, **11**(1), 7–9, 2001.
- Smith, W. H. F., and D. T. Sandwell, Global sea floor topography from satellite altimetry and ship depth soundings, *Science*, **277**, 1956–1962, 1997.
- Taylor, B., and G. D. Karner, On the evolution of marginal basins, *Rev. Geophys.*, **21**, 1727–1741, 1983.
- Taylor, B., K. Crook, and J. Sinton, Extensional transform zones and oblique spreading centers, *J. Geophys. Res.*, **99**, 19,707–19,718, 1994.
- Taylor, B., K. Zellmer, F. Martinez, and A. Goodliffe, Sea-floor spreading in the Lau back-arc basin, *Earth Planet Sci. Lett.*, **144**, 35–40, 1996.
- Tiffin, D. L., Tectonic and structural features of the Pacific/Indo-Australian plate boundary in the North Fiji-Lau Basin regions, southwest Pacific, *Geo Mar. Lett.*, **13**, 126–131, 1993.
- Turner, I. M., C. Peirce, and M. C. Sinha, Seismic imaging of the axial region of the Valu Fa Ridge, Lau Basin-The accretionary process of an intermediate back-arc spreading ridge, *Geophys. J. Int.*, **138**, 495–519, 1999.
- Vallier, T. L., et al., Subalkaline andesite from Valu Fa Ridge, a back-arc spreading center in southern Lau Basin: Petrogenesis, comparative chemistry, and tectonic implications, *Chem. Geol.*, **91**, 227–256, 1991.
- Weissel, J. K., Evolution of the Lau Basin by the growth of small plates, in *Island Arcs Deep Sea Trenches and Back Arc Basins*, *Maurice Ewing Ser.*, vol. 1, edited by M. Talwani and W. C. Pitman, pp. 429–436, AGU, Washington, D. C., 1977.
- Weissel, J. K., Magnetic lineations in marginal basins of the western Pacific, *Philos. Trans. R. Soc. London Ser. A*, **300**, 223–247, 1981.
- Wessel, P., and W. H. F. Smith, Free software helps map and display data, *Eos Trans. AGU*, **72**(41), 441–446, 1991.
- Wetzel, L. R., D. A. Wiens, and M. C. Kleinrock, Evidence from earthquakes for bookshelf faulting at large non-transform offsets, *Nature*, **362**, 235–237, 1993.
- Wiedicke, M., and J. Collier, Morphology of the Valu Fa Spreading Ridge in the Southern Lau Basin, *J. Geophys. Res.*, **98**, 11,769–11,782, 1993.
- Wiedicke, M., and W. Habler, Morphotectonic characteristics of a propagating spreading system in the northern Lau Basin, *J. Geophys. Res.*, **98**, 11,783–11,797, 1993.
- Wilson, D., Motion and deformation of Juan de Fuca Plate, *J. Geophys. Res.*, **98**, 16,053–16,071, 1993.
- Wright, D. J., S. H. Bloomer, C. J. MacLeod, B. Taylor, and A. M. Goodliffe, Bathymetry of the Tonga Trench and Forearc: A map series, *Mar. Geophys. Res.*, **21**, 489–512, 2000.